

Development of an uncertainty-aware equation of state for gold

Lin H. Yang^{1,*} and James A. Gaffney¹

¹*Lawrence Livermore National Laboratory, CA 94551, USA*

This study introduces a framework that employs Gaussian Processes (GPs) to develop high-fidelity equation of state (EOS) tables, essential for modeling material properties across varying temperatures and pressures. GPs offer a robust predictive modeling approach and are especially adept at handling uncertainties systematically. By integrating Error-in-Variables (EIV) into the GP model, we adeptly navigate uncertainties in both input parameters (like temperature and density) and output variables (including pressure and other thermodynamic properties). Our methodology is demonstrated using first-principles density functional theory (DFT) data for gold, observing its properties over maximum density compression (up to 100 g/cc) and extreme temperatures within the warm dense matter region (reaching 300 eV). Furthermore, we assess the resilience of our uncertainty propagation within the resultant EOS tables under various conditions, including data scarcity and the intrinsic noise of experiments and simulations.

PACS numbers:

I. INTRODUCTION

High-fidelity Equation of State (EOS) models are crucial for accurately characterizing material properties under varying temperature and pressure conditions. Key attributes of an EOS include precision, consistency, robustness, and the capacity to predict beyond the calibrated domain. However, the impact of data uncertainty is often overlooked but critical when selecting an EOS. These data are inherently uncertain, with variations from measurement and simulation processes. Integrating these uncertainties into an EOS model poses a compelling challenge. Existing EOS modeling methods such as QEOS/XEOS [1–3] do not account for these data uncertainties, which can result in significant underestimation of the total uncertainty in regions of extrapolation and potential overfitting in the areas of interpolation.

To capture the data uncertainties in the EOS table generation systematically, Ali *et al.* [4] present a methodology

*Corresponding author: lyang@llnl.gov

for robustly propagating uncertainties from experimental data to multi-phase EOS (MEOS) models developed at Lawrence Livermore National Laboratory [5] and then to simulations of application systems, allowing for a high confidence level in predictions based on this methodology. The integration of Monte Carlo methods for uncertainty propagation further enhances the reliability of the results, ensuring that the derived MEOS models incorporate the inherent uncertainties from experimental measurements.

Creating an ensemble of EOS tables directly responds to these uncertainties, providing a spectrum of possible outcomes representing the range of data variability. Despite the success of this method in constructing uncertainty-aware EOS for copper, the primary challenge lies in the efficiency of this approach. Generating hundreds to thousands of EOS tables is computationally intensive, requiring significant resources and time. This could limit the method's practical application, especially when rapid results are needed or when resources are constrained.

Gaussian Processes (GPs) offer a Bayesian kernel-based alternative for modeling and predicting uncertainties, presenting a substantial shift from traditional Monte Carlo methods in the development of EOS. GPs inherently provide predictive variance, furnishing error bars or confidence intervals for each prediction [6]. This capability circumvents the necessity of generating an extensive ensemble of EOS tables, potentially ranging from hundreds to thousands, to represent uncertainty, thereby streamlining the prediction process.

The strengths of GPs in this context include:

- Predictive variance: GPs naturally measure uncertainty with each prediction, which can be interpreted as predictive variance. This feature is precious when it's crucial to quantify the confidence in the model predictions.
- Avoidance of ensembles: Unlike Monte Carlo simulations, which require the generation of a large number of samples to estimate uncertainty, GPs can estimate uncertainty without creating an ensemble of EOS tables. This can significantly reduce computational overhead.
- Flexibility and adaptability: Due to their non-parametric nature, GPs are flexible in modeling complex functions and can adapt their complexity to the data. This makes them suitable for capturing the subtle different behaviors of materials under different conditions without imposing rigid functional forms such as the baseline EOS models [5, 7].
- Incorporating prior information: GPs allow the inclusion of prior knowledge through the choice of kernel functions, which can encode assumptions about the smoothness, periodicity, or other properties of the underlying process, such as the thermodynamic consistency in the EOS construction [8].

- Handling of sparse data: GPs are particularly useful at working with sparse datasets, common in experimental settings where data collection is expensive. Because they can provide detailed uncertainty information, GPs can be more data-efficient, requiring fewer data points to make robust predictions than other methods. The main advantage in the context of EOS development is that GPs can streamline the process by providing a direct estimate of the uncertainty rather than having to interpret the spread of an ensemble of predictions, each is based on slightly different assumptions or input data variations.

In conventional GP models, the presumption is that input variables are noise-free, with uncertainty residing solely in the output observations. However, in this study, we have adopted an Error-in-Variables (EIV) GPs approach [9–12], which acknowledges and incorporates uncertainties in both inputs and outputs to model the inherent uncertainty within the EOS. We will showcase this methodology by analyzing experimental and simulation data for gold, examining the resilience of our uncertainty propagation in the resulting EOS against data scarcity and experimental and simulation noise challenges.

Research into the EOS for gold (Au) has been pivotal in experimental and theoretical studies, given Au’s significant role in diverse scientific and industrial contexts. The Au EOS has undergone extensive investigation through dynamic compression methods, such as shock wave [13–15] and diamond anvil cell (DAC) experiments for static compression [16–22]. These techniques offer physics insights into Au’s compressibility, phase transitions, and thermal behavior under extreme conditions. At the same time, significant efforts have been made on the theoretical front using first-principles calculations, especially within the density functional theory (DFT) framework [23–29]. These models have been increasingly refined, enhancing our predictions of gold’s behavior under high pressures and temperatures.

The synergy of these experimental and theoretical efforts is essential for a comprehensive understanding of the Au EOS, which holds implications for the geophysics and materials science fields. However, despite these advancements, there remain notable discrepancies in the theoretical data, especially at high pressures [23–29], underscoring the need for more precise theoretical predictions. Both experimental and theoretical studies focusing on gold’s pressure-induced behavior, particularly regarding its melting point and structural transformations, are of great interest. Previous investigations have revealed inconsistent results concerning the sequence of gold’s pressure-induced structural transformations, showing deviations from experimental findings. These inconsistencies between theoretical and experimental outcomes pose challenges in advancing the Au EOS, mainly due to uncertainties stemming from these discrepancies.

This paper is devoted to integrating GP methodologies into uncertainty propagation (UP), elucidates their theoretical underpinnings, and discusses their benefits for developing EOS. Our focus in this paper is directed towards

the deployment of an uncertainty-aware EOS generation tool (UEOS) applied to Au, emphasizing the propagation of uncertainty through the EIV-GPs. We outline the fundamental principles of constructing EOS in materials with a specific application to Au. Subsequently, we examine the various sources of uncertainty in the data, encompassing measurement and simulation uncertainties. In conclusion, we propose a strategy for advancing uncertainty through the UEOS framework for Au and discuss the consequential implications of our findings.

II. GAUSSIAN PROCESSES IN THE EQUATION OF STATE: HANDLING INPUT AND OUTPUT NOISE WITH SQUARED EXPONENTIAL KERNELS

GPs present a formidable option for the propagation of uncertainties in the development and construction of EOS tables. EIV-GPs distinguish themselves by inherently accounting for noise in both inputs and outputs within the model, thereby offering a predictive paradigm that avoids the reliance on ensemble tables commonly necessitated by Monte Carlo simulations. This section elucidates the employment of EIV-GPs with a squared exponential kernel in constructing EOS tables, with a focus on the computation of predictive means and variances, as well as the significance and application of derivatives within the EIV-GPs framework.

At their core, GPs define a prior over functions and, given data, infer a posterior function space that captures the underlying data-generating process [6, 30]. The kernel or covariance function characterizes the smoothness and variation of these functions, embodying the GP’s assumption about the data correlation. In EOS development, the underlying experimental and theoretical data are often contaminated with noise. EIV-GPs [9–12] address this by modeling the noise directly in the training data set that a local linear Taylor expansion about each input point is used. This approach allows the input noise to be reformulated as output noise proportional to the squared gradient of the GP posterior mean. The formulation of the EIV-GPs approach is detailed in the Appendix section.

We have implemented the EIV-GPs methodology in the uncertainty-aware EOS outlined via a flow chart in Fig. 1. The workflow takes simulation or experimental data and their respective uncertainties into GP kernels alongside a designated optimization scheme. This integration precipitates the hyperparameter optimization within the UEOS engine. After this optimization, GP and UP operations are employed, which encompasses derivatives, additions, and subtractions. These operations are pivotal in determining the resulting internal energy, Helmholtz, and Gibbs free energies, each appended with predictive uncertainties. The derived uncertainties and their mean values, indicative of the EOS energies, can then be looped back into the UEOS engine to extrapolate additional thermodynamic properties.

GPs are inherently adaptive due to their *non-parametric* nature, which allows them to model complex functions and

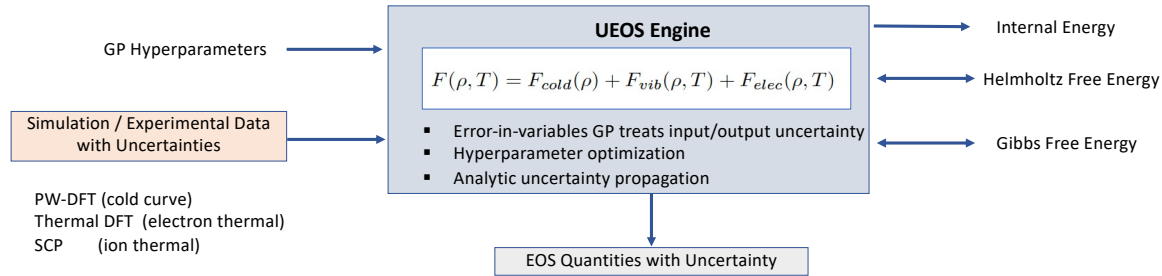


FIG. 1: Schematic flow chart outlining the general process for the UEOS. The process starts with simulation/experiment data and uncertainties feeding into GP kernels and an optimization scheme, leading to the UEOS engine’s hyperparameter optimization. This optimization is connected to GP and UP operations, such as derivatives, additions, and subtractions, that influence the resulting energies.

tailor their complexity to the specifics of the data. This adaptability renders them particularly effective for capturing the complex behavior of materials under varying conditions without the constraints of rigid functional forms, such as those imposed by the Vinet EOS model [31], a widely recognized standard in EOS modeling [7]. Figure 2 exemplifies the versatility of the UEOS engine in concurrently constructing the energy vs. density and pressure vs. density equation of states, along with the uncertainties predicted and propagated from the DFT cold energy data.

The UEOS tool offers a compelling approach for handling measurement and simulation uncertainties in GPs by explicitly introducing latent variables and probability distributions to model input and output errors. This allows for more accurate predictions and a better understanding of the underlying system. Additionally, it provides a way to estimate measurement and simulation uncertainties, which can be useful for identifying and correcting errors in measurements and simulations. This approach facilitates the estimation of uncertainties in both measurements and simulations, providing instrumental help in identifying and amending errors within these domains. Figure3 exemplifies this application, demonstrating the correlation between simulation data and experimental results. The analysis incorporates input uncertainties (such as densities) from experiments and compares them against outputs (like pressure) obtained from simulations and experimental procedures [32, 33]. This integrated analysis underscores the synergy between experimental data and computational models, enhancing the accuracy and reliability of scientific findings.

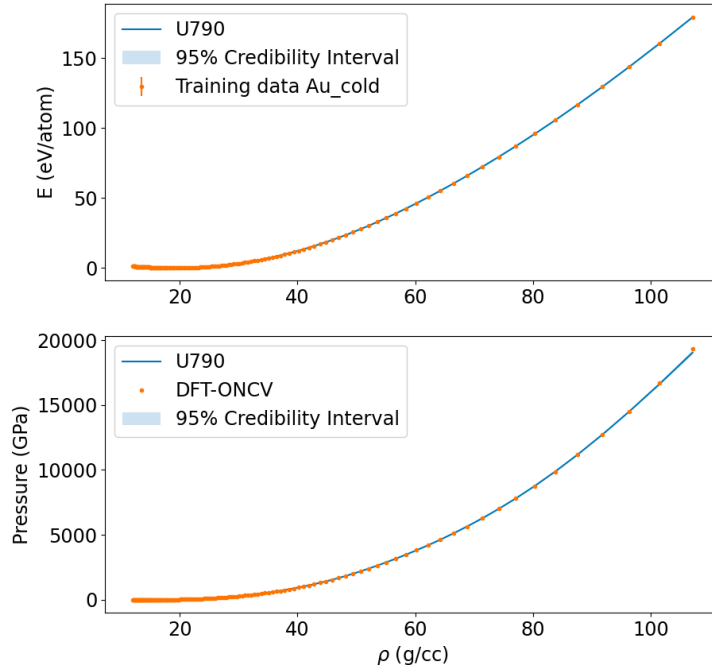


FIG. 2: The Au EOS is derived by inputting DFT data into EIV-GPs. This process facilitates the automatic computation of the derivative of the cold energy with respect to density, incorporating the predicted uncertainties within the model’s output

III. FIRST-PRINCIPLES HELMHOLTZ FREE ENERGY FOR GOLD

We conduct a detailed analysis of the system’s free energies in developing our EOS for Au. This analysis deliberately excludes consideration of electron-phonon coupling at finite temperatures. Instead, we categorize free energy into ground-state (cold), electron-thermal, and ion-thermal terms. Each component uniquely reflects the system’s characteristics under varying thermal and pressure conditions. For precise derivation of these energies, we have utilized plane-wave pseudopotential methods [34, 35] within the DFT. We employed a range of exchange-correlation functionals, including the local density approximation (LDA) [36], Perdew-Burke-Ernzerhof (PBE) [37, 38], PBE for solids (PBEsol) [39], and relativistic effects [40, 41], crucial for ensuring a comprehensive and accurate representation of the system’s behavior. Furthermore, by exploring different exchange-correlation forms within DFT, we enhance our ability to assess uncertainties, thus providing a more robust understanding of the system’s properties under various thermal and pressure conditions. We utilized Born-Oppenheimer Molecular Dynamics (BOMD) simulations to probe low-temperature liquid states. Further enhancing our approach, we incorporated the self-consistent phonon technique to precisely quantify the contributions of temperature-dependent thermal vibrations, a method thoroughly developed

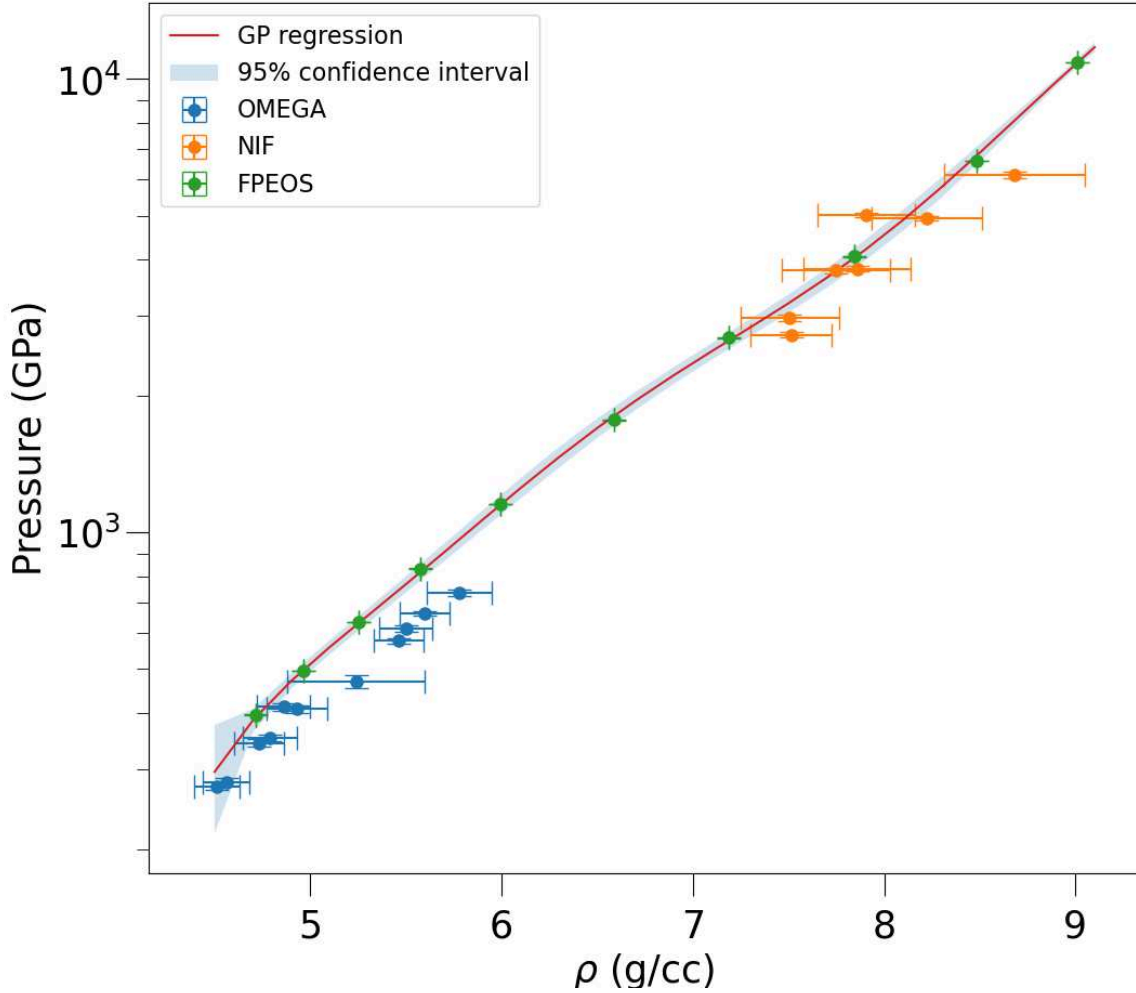


FIG. 3: EIV-GPs present a sophisticated method for correlating uncertainties derived from simulations and experiments. The plot illustrates the predicted mean and confidence intervals of the Hugoniot curve for B_4C from theoretical database, FPEOS [33], and experimental results [32]. This methodology enhances the understanding of discrepancies between theoretical predictions and experimental data, enabling the identification and correction of potential errors in both measurement and simulation processes.

by Tadano *et al.* [42].

To accommodate the broad range of densities ($0.5\rho_0 - 5\rho_0$) and temperatures (up to 300 eV) for the Au EOS table, we have generated an optimized norm-conserving Vanderbilt pseudopotential (ONCVpsp) [43, 44]. This Au ONCVpsp, comprising a total of 33 valence states ($4f^{14}, 5s^2, 5p^6, 5d^{10}, 6s^1$) and local potential cutoff radius of $r_c = 1.1$ bohr demonstrates both accuracy and efficiency in generating the DFT data necessary for constructing the Au EOS. This pseudopotential's accuracy is affirmed by comparing bulk properties with existing theoretical and experimental

results, as illustrated in Table II. The extensive valence state configuration ensures transferability under extremely high pressure and temperature conditions due to electron excitation. Additionally, to guarantee the self-consistent convergences of total energy to less than one meV per atom and pressure in $kbars$, we have set the plane-wave kinetic-energy cutoff at 175 Hartree.

TABLE I: Comparison of equilibrium volume V_0 , bulk modulus B_0 , and its pressure derivative B'_0 obtained through various exchange-correlation functionals (LDA, PBE, PBEsol, and spin-orbit coupling). Among these, PBEsol and PBEsol with S-O coupling yielded the most accurate results.

XC functional	V_0 (\AA^3)	ρ_0 (g/cc)	B_0 (GPa)	B'_0
LDA	16.57	19.72	194	5.61
PBE	17.96	18.20	139	5.83
PBEsol	17.00	19.22	175	5.90
LDA+SO	16.46	19.85	199	5.78
PBE+SO	17.81	18.35	144	5.83
PBEsol+SO	16.92	19.31	179	5.88

TABLE II: Comparison of equilibrium volume V_0 , bulk modulus B_0 , and its pressure derivative B'_0 obtained through various methods. The findings reported here are based on these optimal outcomes from the PBEsol functional.

Method	V_0 (\AA^3)	B_0 (GPa)	B'_0
ONCV _{psp}	17.00	175	5.90
FP-LMTO [29]	17.10	171	5.78
Exp.			
T = 300 K [21]	16.96	167	5.88
T = 0 K [45]		180	

The Helmholtz free energy ($F = U - TS$) for each phase is a sum of three terms:

$$F(\rho, T) = F_{cold}(\rho) + F_{vib}(\rho, T) + F_{elec}(\rho, T)$$

, where F_{cold} is the total energy at $T=0$ for the crystalline phase, F_{vib} is the ion-thermal contribution from the thermal vibration of ions in solids and liquids, and F_{elec} represents the electron-thermal contribution from excited electrons.

In our current work, we aim to showcase the construction of the Au EOS using the UEOS tool, with a primary focus on the solid face-centered cubic (fcc) phase and the liquid phase. This targeted approach is in preparation for

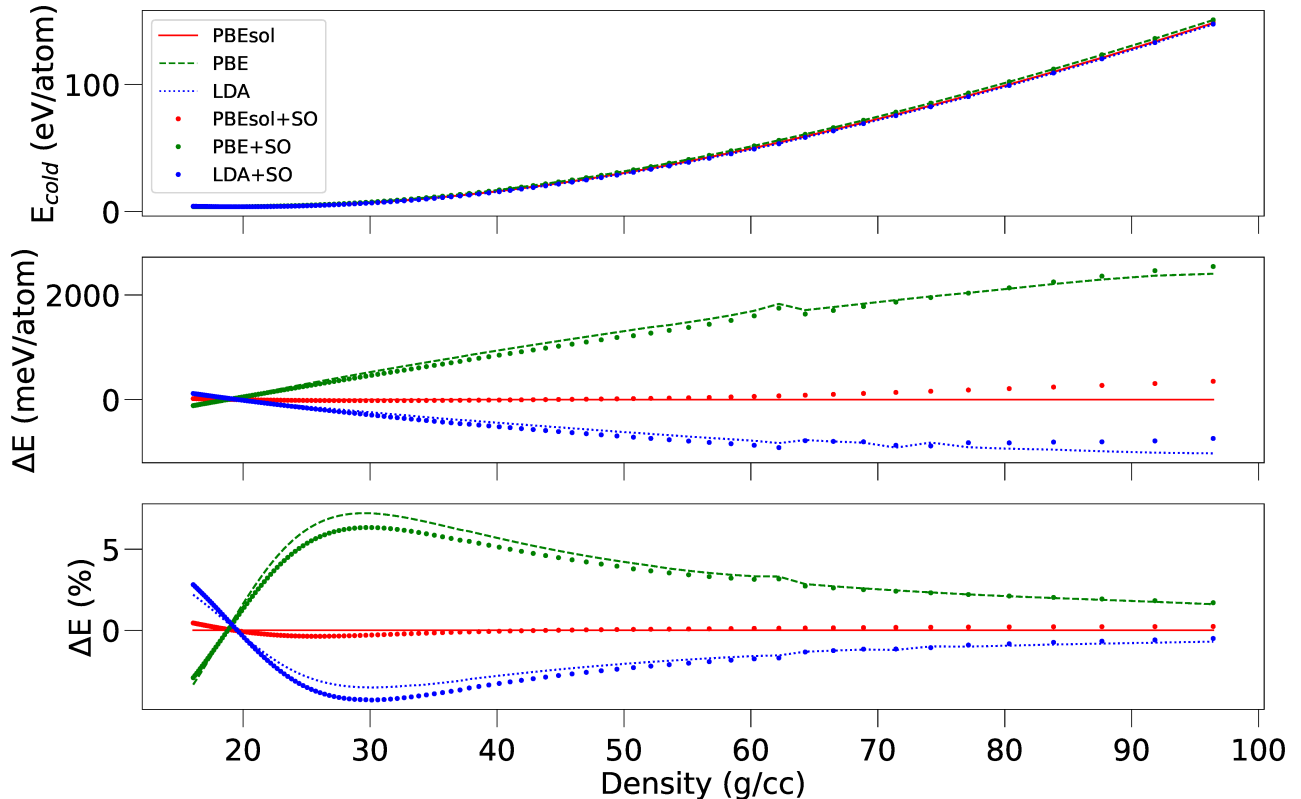


FIG. 4: Comparison of cold EOS's for fcc Au using different density functional forms and S-O coupling. For the energy difference, we use PBEsol as the reference.

a more extensive exploration, which will be detailed in a forthcoming paper [46]. We will present the multiphase Au EOS and the corresponding thermodynamic properties in that comprehensive study. This step-by-step examination allows for a more precise understanding and systematic development of the Au EOS, setting the stage for the broader, in-depth analysis planned for subsequent publication.

This section outlines the methodology employed to derive the Helmholtz free energy from DFT calculations.

A. Ground state energy

The ground state energies of fcc solids were calculated using DFT within the framework of plane-wave pseudopotentials. We utilized various exchange-correlation functionals within the DFT framework, including LDA, PBE, PBEsol, and the relativistic effect. Table I lists the equilibrium bulk properties of Au based on various DFT functionals. Among these, PBEsol and PBEsol with S-O coupling yielded the most accurate bulk properties, as indicated in

Table II.

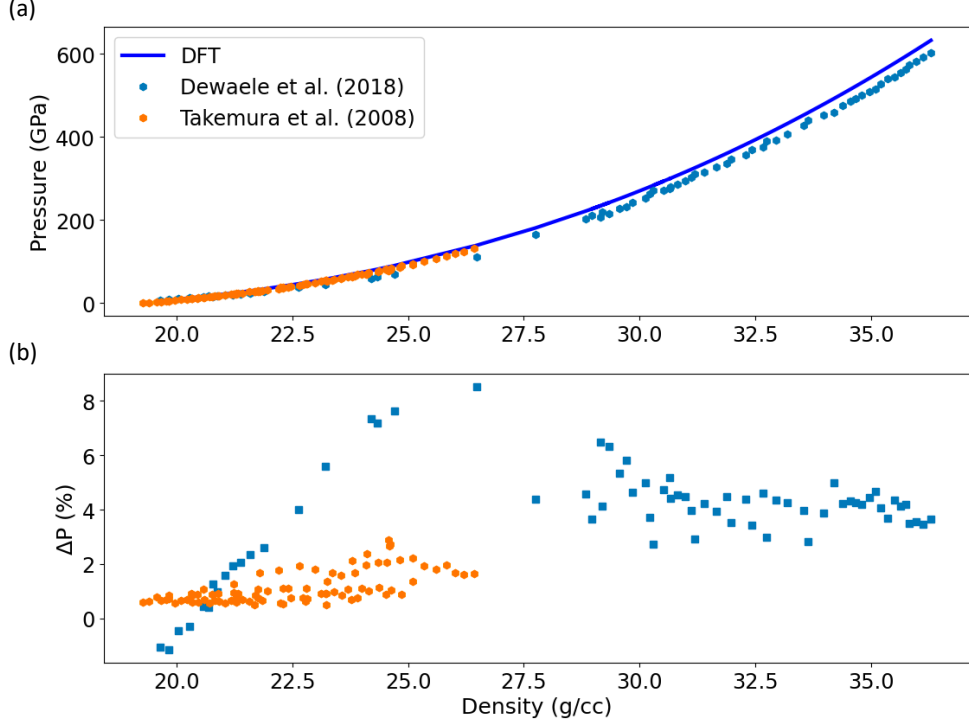


FIG. 5: (a) Au isotherm data from DFT calculations (solid line), DAC [22] (orange hexagons) and tDAC [20] (blue squares) measurements. (b) The percent difference between DFT isotherm data and experiments.

We performed an in-depth comparison of isotherm pressure against density using our DFT calculations and diamond anvil cell (DAC) data [22], over a density span of 19.28 (ρ_0) to 26.5 g/cc. This analysis examined the pressure differences between our DFT results and the DAC data. The outcomes demonstrate a notable alignment between the two, with an overall consistency within a 2.5% margin, as depicted in Figure 5 (b). Additionally, we extended our comparison to higher pressures, reaching up to 600 GPa (36 g/cc), by contrasting our DFT data with recent findings using a toroidal diamond anvil cell (tDAC), as reported by Dewaele *et al.* [20]. In these high-pressure conditions, the discrepancies between DFT and tDAC data become more pronounced, culminating in differences as large as 8% around 27 g/cc.

B. Electron-thermal free energy

In our study, akin to the approach used in ground-state calculations for solids, we determined the electron-thermal free energy by solving the Kohn-Sham equation, integrating Fermi-Dirac statistics to model electron occupancy at

finite temperatures. We selected the face-centered cubic (fcc) solid at $T = 0$ K as the reference configuration for ions. We computed both the internal energy, $U_{ele}(\rho, T)$, and the free energy, $F_{ele}(\rho, T)$, in a self-consistent manner across each density (ρ) and temperature (T) grid point. Additionally, we incorporated snapshots from BOMD simulations as alternate reference configurations for ions. This method enabled us to evaluate the uncertainties associated with the electron-thermal free energy, particularly those arising from variations in electron occupation at finite temperatures.

C. Ion-thermal free energy

To calculate Helmholtz free energy F_{vib} and internal energy U_{vib} , we employed self-consistent phonon (SCP) calculations. The SCP theory is used for calculating temperature-dependent phonon frequencies nonperturbatively. This involves assuming an effective harmonic phonon frequency and a polarization vector, which are used to define an effective harmonic Hamiltonian. The renormalized phonon frequencies and eigenvectors are determined to minimize the vibrational free energy within the first-order cumulant approximation. The SCP theory involves dealing with the anharmonic system described by a Hamiltonian includes a harmonic part and anharmonic terms of different orders. While SCP accounts for quartic anharmonicity, it neglects cubic anharmonicity. Improved self-consistent (ISC) phonon theory, however, includes an additional three-phonon term perturbatively. This is expressed as the Helmholtz free energy from a bubble diagram associated with cubic anharmonicity [42].

a. Vibration free energies for solids Within the framework of SCP theory, the extraction of second, third, and fourth-order interatomic force constants (IFCs) is achieved through first-principles calculations. This process entails systematically displacing atoms within a supercell and subsequently computing the forces that arise from these displacements. The resulting data are then fitted to accurately estimate the force constants. Specifically, for fcc Au, we conducted 65 distinct atomic displacements in a supercell comprising 64 atoms at each density to determine these force constants. We have examined the simulation size effects on the energy by employing a supercell containing 108 and 256 atoms, respectively. The discrepancy is less than 1% on average for the density range we presented in this work. The uncertainty due to the choice of simulation sizes will be addressed in Sec.IV. Additionally, the anharmonic IFCs are derived using the Compressive Sensing Lattice Dynamics (CSLD) method [42, 47].

The SCP equation is solved using numerical algorithms such as the least absolute shrinkage and selection operator (LASSO) technique. The \mathbf{q} mesh ($4 \times 4 \times 4$) of the SCP is set commensurate with the supercell size, and an inner \mathbf{q} mesh is increased for convergence of anharmonic phonon frequencies. Effective dynamical matrices are converted into real-space effective second-order IFCs, which are used to calculate anharmonic phonon frequencies on a denser

\mathbf{q} -point grid. For Au fcc solid, a $(51 \times 51 \times 51)$ \mathbf{q} -point grid is employed.

Utilizing SCP theory to compute the ion-thermal free energy offers a notable advantage over BOMD, as it maintains the crystalline symmetry in solids. Simultaneously, SCP theory efficiently calculates the vibration free energy.

b. Vibration free energies for liquid For low-temperature liquids, our SCP calculations are based on configurations sampled from BOMD simulations. We have calculated the finite-temperature IFCs and frequencies using the SCP method, which was previously detailed for the solid phase. To extend the internal and free energy models of the SCP to higher temperatures in the warm dense matter region, we used the cell model [5, 7], which enforces an ideal gas limit for $C_V^{ion} \rightarrow \frac{3}{2}k_B T/atom$ as $T \rightarrow \infty$. This free-energy model is represented by the following equations:

$$F_{\text{vib,liquid}}(\rho, T) = F_{\text{vib,solid}}(\rho, T) - k_B T \ln \left[\text{erf} \left(\frac{T^*}{T} \right) - \frac{2}{\sqrt{\pi}} \sqrt{\frac{T^*}{T}} \exp \left(-\frac{T^*}{T} \right) \right],$$

where $k_B T^*$ is the ρ -dependent energy defined in the cell-model [5, 7].

$$k_B T^*(\rho) = \frac{M k_B^2 [\theta(\rho) R(\rho)]^2}{2 \hbar^2},$$

$\theta(\rho)$ is ρ -dependent Debye temperature derived from DFT ρ -dependent elastic constants (Fig. 6) and

$$R(\rho) = \left(\frac{3M}{4\pi\rho} \right)^{\frac{1}{3}}.$$

For the internal energy, we adopt the following equation so it satisfies the ideal gas limit as $T \rightarrow \infty$:

$$U_{\text{vib,liquid}}(\rho, T) = U_{\text{vib,solid}}(\rho, T) \left[\frac{1}{2} + \frac{1}{2} \exp \left(-\sqrt{\frac{T}{T^*}} \right) \right],$$

This approach allows for a more comprehensive modeling of internal and free energies across various temperature ranges.

IV. SOURCES OF DFT DATA UNCERTAINTY

Uncertainty quantification (UQ) in DFT calculations is paramount in assessing the credibility and precision of simulation outcomes. In these calculations, many factors contribute to uncertainty, encompassing the choice of exchange-correlation functionals, various numerical approximations (including distinct algorithms for solving the Kohn-Sham equation), and establishing convergence criteria. Consequently, a continuous and dedicated research effort is aimed at quantifying and reducing these uncertainties to enhance the fidelity of DFT simulations [49–52].

Benchmarking plays a pivotal role in evaluating the uncertainties associated with DFT techniques. It involves comparisons of computed properties with experimental data or high-precision theoretical models such as quantum

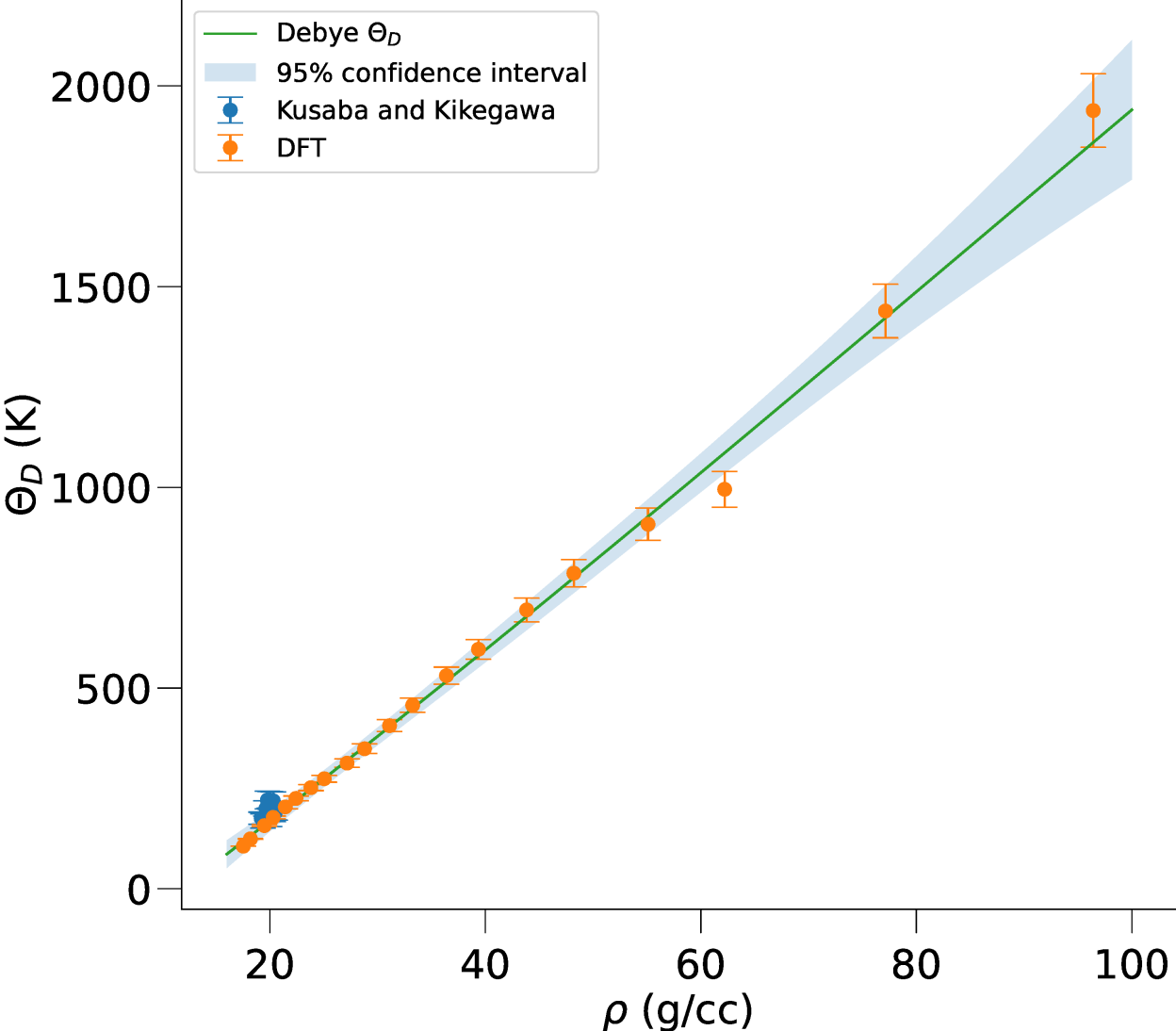


FIG. 6: Debye temperature of gold as a function of density from DFT calculations (orange dots) and experimental data [48]. The blue solid line represents a Gaussian Process (GP) fit, with the 95% confidence interval indicated by the shaded region.

Monte Carlo or advanced all-electron electron-structure methods. In our pursuit of benchmarking against experimental data and the all-electron FP-LMTO method [53], for the ground-state EOS, we have undertaken a comprehensive approach. This approach extends to utilizing two distinct pseudopotential plane-wave codes [34, 35], strategically chosen to probe potential discrepancies stemming from divergent numerical algorithms.

The examination of property convergence, considering both the basis set's size and the simulation's dimensions (number of atoms), is a pivotal aspect of our uncertainty assessment. In practice, utilizing larger basis sets or

supercell dimensions frequently enhances result accuracy, albeit at the cost of increased computational resources. To ascertain the limits of basis set sizes and supercell dimensions and to quantify the accompanying errors, we consistently integrate basis set extrapolation techniques as a fundamental and standard element of our analytical methodologies.

TABLE III: Sources of uncertainty in our DFT free-energy training data for the development of UEOS table for Au. Exp.-Theory accounts for the model discrepancy between DFT data and experiments. The assessments on the theory side includes simulation size effect, BOMD configuration samplings and higher order terms for the SCP calculations.

Source of uncertainty	U_{cold}	F_{elec}	$F_{vib,gha}$	$\Delta F_{vib,ah}$
Exp.-Theory	5%		1%	3%
Theory	1%	1%	2%	4%

Additional sources of uncertainty in our analyses include the incorporation of higher-order terms in SCP calculations, statistical sampling through BOMD for electron-thermal properties, and using SCP calculations to model the liquid state. These factors introduce complexity and potential variations in our results, necessitating careful consideration and thorough quantification of their impact on our overall uncertainty assessment.

The various sources of uncertainties related to the generation of our DFT database are comprehensively outlined in Table III. We have meticulously integrated these uncertainties into EIV-GPs to create an uncertainty-aware EOS table for Au.

V. UNCERTAINTY-AWARE EOS FOR GOLD

The EOS table is meticulously constructed by evaluating the free energy across a comprehensive grid of temperatures and densities, utilizing the UEOS tool, as depicted in Fig. 1. At each grid point, we derive the pressure (P) and other thermodynamic properties directly from the Helmholtz free energy. For example, the thermal pressure P is calculated using the equation:

$$P(\rho, T) = \frac{\rho^2}{M} \left(\frac{\partial F(\rho, T)}{\partial \rho} \right)_T$$

Here, M represents the total mass in the system. This pressure calculation uses the energy-density isotherm via EIV-GP engine, as demonstrated in Fig. 2.

Furthermore, the Gibbs free energy $G(\rho, T)$, which is defined as $G(\rho, T) = F(\rho, T) + P(\rho, T)\frac{M}{\rho}$, simplifies to $G(\rho, T) = F(\rho, T) + \rho \left(\frac{\partial F(\rho, T)}{\partial \rho} \right)_T$. This allows for a direct evaluation of the Gibbs free energy from Helmholtz

free energy $F(\rho, T)$ within the EIV-GP framework, ensuring a robust and accurate determination of these critical thermodynamic quantities with predicted uncertainties propagated from the free energy.

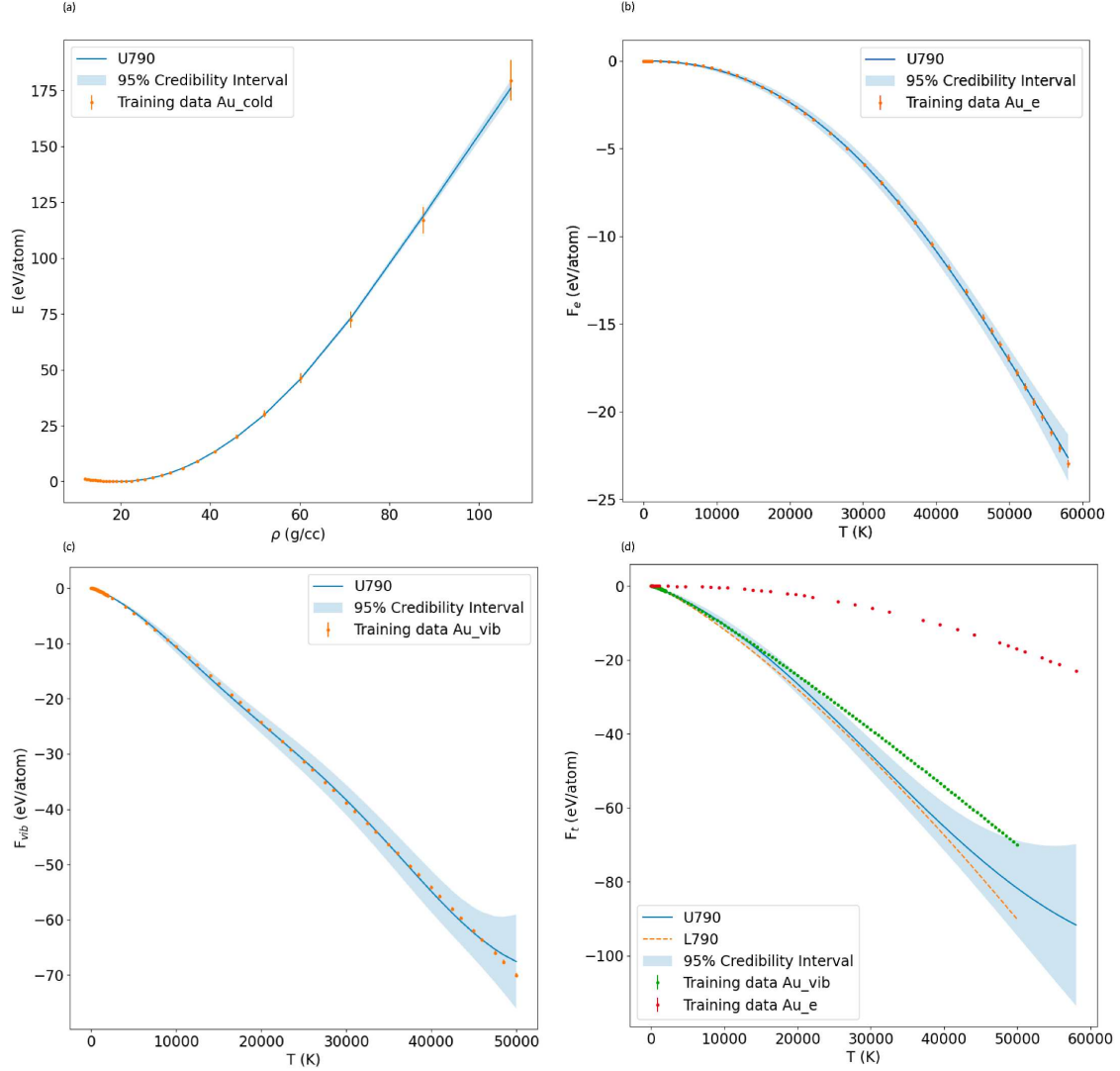


FIG. 7: The total free energy with predicted uncertainty is constructed using EIV-GP engine. The engine takes the free energy components: (a) cold energy, (b) electron-thermal free energy, and (c) ion-thermal free energy with uncertainties as training data and processes them to generate (d) the total free energy with predicted uncertainty.

A. Helmholtz free energy with predicted uncertainties

Figure 7 illustrates the method of computing the Helmholtz free energy, denoted as $F(\rho = 2\rho_0, T)$, over a temperature range from 0 to over 50,000 K. To construct the total free energy along with its predicted uncertainty, we utilize the EIV-GP engine. This engine operates by taking the individual components of free energy, each accompanied by their respective uncertainties, as input data. It then processes these inputs to generate a comprehensive total free energy, complete with a quantified uncertainty prediction.

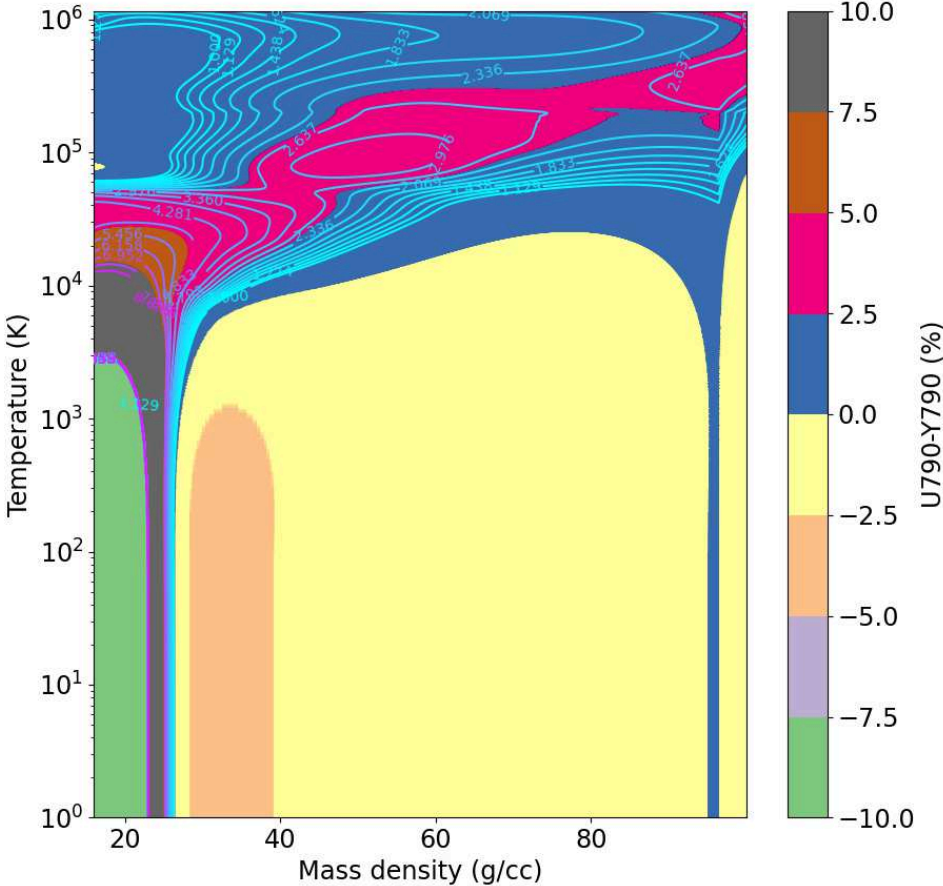


FIG. 8: Helmholtz free energy comparison between U790 and Y790. Across a broad spectrum of densities, ranging from 16 g/cc to 100 g/cc, and temperatures spanning from 0 K to 10^6 K. The comparative analysis reveals that the agreement between Y790 and U790 remains within a narrow margin of less than 10%.

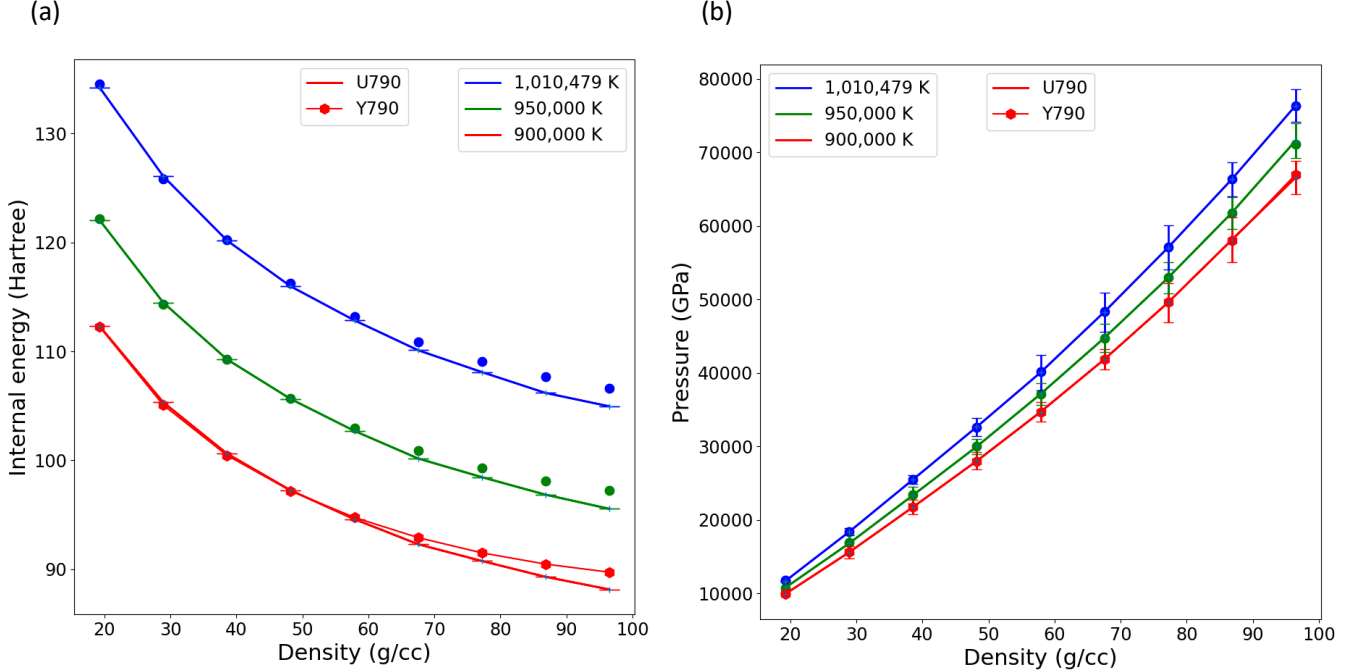


FIG. 9: (a) Comparing the internal energy of U790 and Y790, a notable consistency is observed across various densities (16 to 100 g/cc) and at specific temperatures (900,000 K, 950,000 K, and 1,010,479 K). (b) Total thermal pressure comparison between U790 and Y790.

B. Comparisons with L790 and Y790

Comparative analysis of the newly developed U790 is essential, particularly when compared with the well-established EOS table for Au. Here, we specifically focus on contrasting the Helmholtz free energy profiles between the recently developed U790 and the Lawrence Livermore National Laboratory (LLNL) L790 and Y790 EOS tables. It is important to note that the L790 is based on the Thomas-Fermi electron-thermal model, while Y790 was generated from the Purgatonio electron-thermal model. These fundamental differences in the modeling approach account for the observed discrepancies between U790 and these two well-established tables. Such disparities, while expected, offer valuable insights into the limitations and applicability of each model, especially in high-pressure and high-temperature conditions where precise EOS data is crucial. This close correlation underscores the reliability and accuracy of the proposed U790 table in replicating the thermodynamic properties of materials under a wide range of extreme conditions. This comparison not only underscores each model's unique characteristics but also aids in refining our understanding of materials' behavior under extreme conditions.

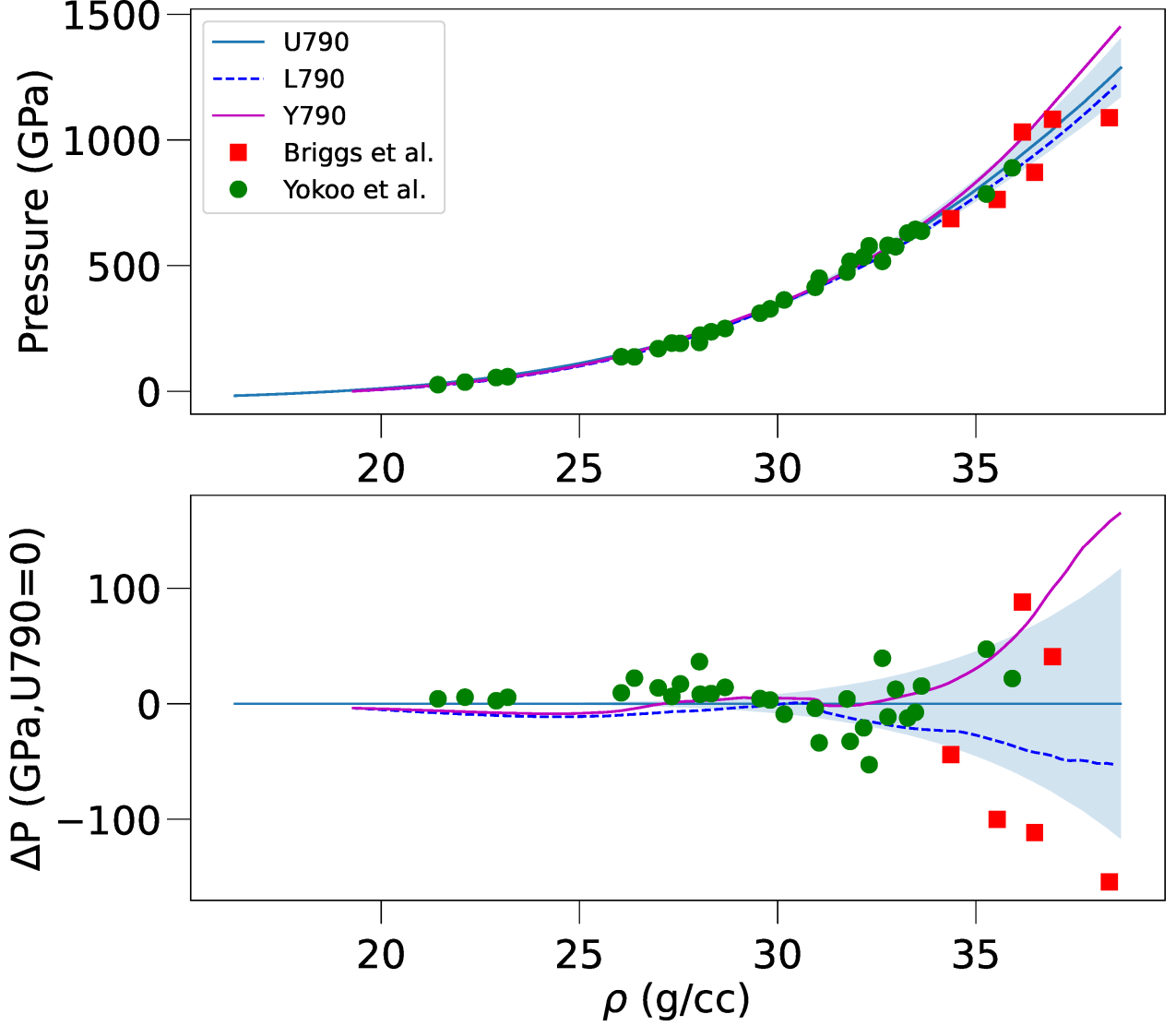


FIG. 10: Comparison of shock Hugoniot (pressure versus density) from the initial density $\rho_0 = 19.28$ g/cc calculated in this work (U790), L790, Y790 and experiments in the literature [13, 14] show the alignment of current results with established benchmarks in the field.

C. Shock Hugoniot comparison

One key property derived from the EOS table is the shock Hugoniot data, which is obtained by solving the Rankine-Hugoniot equation. This equation encompasses the internal energy, density, and pressure. Benchmarking the Hugoniot data against existing EOS tables and experimental results is an essential aspect of the validation process.

Figure 10, which displays the Hugoniot pressure versus density, clearly exhibits a significant correlation with the

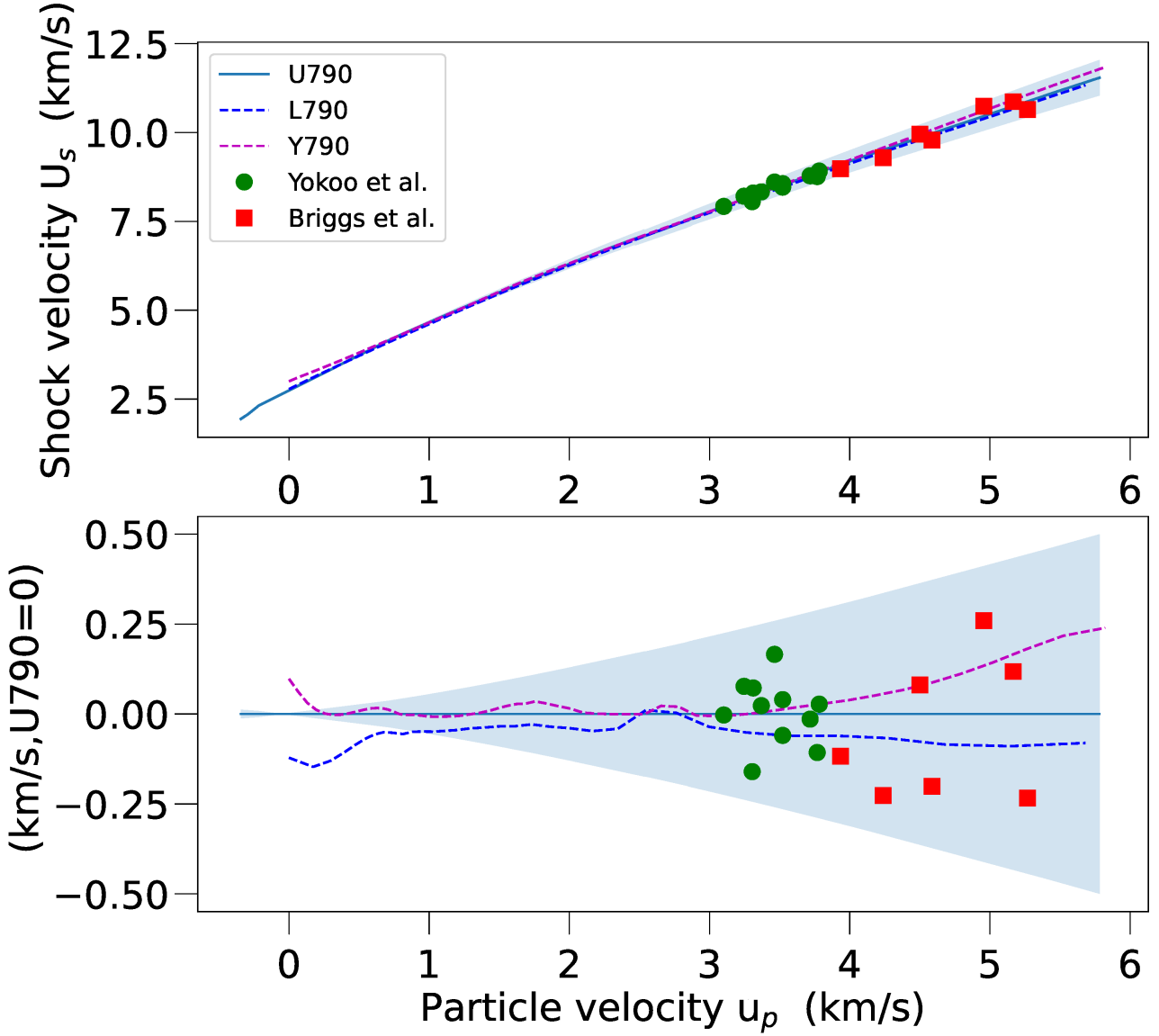


FIG. 11: Comparison of shock Hugoniot U_s - u_p relation from the initial density $\rho_0 = 19.28 \text{ g/cc}$ calculated in this work (U790), L790, Y790 and experiments in the literature [13, 14].

L790 and Y790 and experimental findings [13, 14]. This consistency validates the current methodologies for calculating Hugoniot pressure across various densities, affirming their accuracy in line with established models like the L790 and Y790.

Furthermore, Figure 11 explores the relationship between shock velocity and particle velocity, providing additional support for the validity of the current approach. The close alignment of these results with both the L790, Y790 and existing experimental data serves as a testament to the precision and reliability of UEOS tool.

In summary, our Hugoniot data underscore the capability of UEOS tool in accurately reproducing and understanding intricate physical phenomena, especially in the field of high-pressure physics. The agreement between new findings and well-established data is pivotal for propelling the field forward, offering a solid basis for future investigations and potential applications in the plasma physics field.

VI. CONCLUSIONS

A key idea in our methodology is integrating the Error-in-Variables (EIV) approach into the Gaussian Process (GP) model. This strategy adeptly manages uncertainties inherent in both input parameters (such as temperature and density) and output variables (including pressure and other thermodynamic properties). The robustness of our approach is demonstrated through its application to first-principles density-functional-theory (DFT) data for gold, meticulously examining its behavior at maximum density compression (up to 100 g/cc) and extreme temperatures within the plasma region (up to 100 eV). Moreover, we critically evaluated the resilience of our uncertainty propagation techniques within the generated EOS tables under various challenging scenarios, including data scarcity and the intrinsic noise of experimental and simulation data.

However, our study also acknowledges the computational cost and limitations inherent in using GPs. While they are incredibly versatile in modeling complex functions and tracking uncertainty, their scalability to large datasets is a significant challenge. The primary constraint is the $O(N^3)$ computation cost, required for matrix factorization to evaluate marginal likelihoods and make predictions. Additionally, the computational burden of kernel matrix calculations $O(DN^2)$, D is the dimension of input data, and the extensive memory requirements $O(N^2)$ can be substantial, often imposing a hard limit on the size of problems that can be tackled. While there exists a rich body of literature on special cases and approximations of GPs that are more computationally efficient, these models are not without their limitations. For instance, certain functions cannot be represented accurately by a Gaussian process, and any deviation from Gaussian observation processes necessitates additional approximations and computational work.

In conclusion, our work illustrates the potential of integrating advanced statistical methods like EIV-GP into material science research, especially in constructing comprehensive EOS tables. Despite the computational challenges, the benefits of such approaches in accurately modeling material behavior under extreme conditions are undeniable. Future research should focus on optimizing these models for greater computational efficiency and exploring their application in a broader range of materials and conditions.

VII. ACKNOWLEDGMENTS

We thank Drs. Suzanne Ali, John Pask, Per Söderlind, and Phil Sterne, for their valuable discussions. This work was performed under the auspices of the U.S. Department of Energy by Lawrence Livermore National Laboratory under Contract No. DE-AC52-07NA27344.

VIII. REFERENCES

- [1] R. M. More, K. H. Warren, D. A. Young, and G. B. Zimmerman, *The Physics of Fluids* **31**, 3059 (1988), ISSN 0031-9171, https://pubs.aip.org/aip/pfl/article-pdf/31/10/3059/12484353/3059_1_online.pdf, URL <https://doi.org/10.1063/1.866963>.
- [2] D. A. Young and E. M. Corey, *Journal of Applied Physics* **78**, 3748 (1995), ISSN 0021-8979, https://pubs.aip.org/aip/jap/article-pdf/78/6/3748/8045523/3748_1_online.pdf, URL <https://doi.org/10.1063/1.359955>.
- [3] C. J. Wu, D. A. Young, P. A. Sterne, and P. C. Myint, *The Journal of Chemical Physics* **151**, 224505 (2019), ISSN 0021-9606, https://pubs.aip.org/aip/jcp/article-pdf/doi/10.1063/1.5128127/13332097/224505_1_online.pdf, URL <https://doi.org/10.1063/1.5128127>.
- [4] S. J. Ali, D. C. Swift, C. J. Wu, and R. G. Kraus, *Journal of Applied Physics* **128**, 185902 (2020), ISSN 0021-8979, https://pubs.aip.org/aip/jap/article-pdf/doi/10.1063/5.0029723/15258153/185902_1_online.pdf, URL <https://doi.org/10.1063/5.0029723>.
- [5] C. J. Wu, P. C. Myint, J. E. Pask, C. J. Prisbrey, A. A. Correa, P. Suryanarayana, and J. B. Varley, *The Journal of Physical Chemistry A* **125**, 1610 (2021), ISSN 1089-5639, doi: 10.1021/acs.jpca.0c09809, URL <https://doi.org/10.1021/acs.jpca.0c09809>.
- [6] C. E. Rasmussen and C. K. I. Williams, *Gaussian Processes for Machine Learning* (The MIT Press, 2005), ISBN 9780262256834, URL <https://doi.org/10.7551/mitpress/3206.001.0001>.
- [7] C. J. Wu, L. X. Benedict, P. C. Myint, S. Hamel, C. J. Prisbrey, and J. R. Leek, *Phys. Rev. B* **108**, 014102 (2023), URL <https://link.aps.org/doi/10.1103/PhysRevB.108.014102>.
- [8] J. A. Gaffney, Private communication (2023).
- [9] A. Girard and R. Murray-Smith (2003).
- [10] R. Murray-Smith and R. Shorten, eds., *Gaussian Processes: Prediction at a Noisy Input and Application to Iterative*

Multiple-Step Ahead Forecasting of Time-Series (Springer Berlin Heidelberg, Berlin, Heidelberg, 2005), pp. 158–184, ISBN 978-3-540-30560-6, URL https://doi.org/10.1007/978-3-540-30560-6_7.

- [11] A. McHutchon and C. Rasmussen, *Advances in neural information processing systems* **24** (2011).
- [12] J. E. Johnson, V. Laparra, and G. Camps-Valls, *IEEE Geoscience and Remote Sensing Letters* **17**, 391 (2020).
- [13] M. Yokoo, N. Kawai, K. G. Nakamura, and K.-i. Kondo, *Applied Physics Letters* **92**, 051901 (2008), ISSN 0003-6951, https://pubs.aip.org/aip/apl/article-pdf/doi/10.1063/1.2840189/14660864/051901_1_online.pdf, URL <https://doi.org/10.1063/1.2840189>.
- [14] R. Briggs, F. Coppari, M. G. Gorman, R. F. Smith, S. J. Tracy, A. L. Coleman, A. Fernandez-Pañella, M. Millot, J. H. Eggert, and D. E. Fratanduono, *PHYSICAL REVIEW LETTERS* **123** (2019).
- [15] S. K. Han, R. F. Smith, D. Kim, J. K. Wicks, J. R. Rygg, A. Lazicki, J. H. Eggert, and T. S. Duffy, *PHYSICAL REVIEW B* **103** (2021).
- [16] W. Mao, H. Mao, P. Bell, A. Goncharov, V. Struzhkin, and R. Hemley, *Physical Review B* **66** (2002).
- [17] H. K. Yuichi Akahama and A. K. Singh, *Journal of Applied Physics* **92**, 6 (2002).
- [18] S.-H. Shim, T. S. Duffy, and K. Takemura, *Earth and Planetary Science Letters* **203**, 729 (2002), ISSN 0012-821X, URL <https://www.sciencedirect.com/science/article/pii/S0012821X02009172>.
- [19] A. Dewaele, P. Loubeyre, and M. Mezouar, *Physical Review B* **70**, 094112 (2004).
- [20] A. Dewaele, P. Loubeyre, F. Occelli, O. Marie, and M. Mezouar, *Nature Communications* **9**, 2913 (2018), ISSN 2041-1723, URL <https://doi.org/10.1038/s41467-018-05294-2>.
- [21] A. Dewaele and P. Loubeyre, *High Pressure Research* **27**, 419 (2007), <https://doi.org/10.1080/08957950701659627>, URL <https://doi.org/10.1080/08957950701659627>.
- [22] K. Takemura and A. Dewael, *Phys. Rev. B* **78** (2008).
- [23] P. Söderlind, *Phys. Rev. B* **66** (2002).
- [24] L. Dubrovinsky, N. Dubrovinskaia, W. A. Crichton, A. S. Mikhaylushkin, S. I. Simak, I. A. Abrikosov, J. S. De Almeida, R. Ahuja, W. Luo, and B. Johansson, *Physical Review Letters* **98**, 045503 (2007), ISSN 0031-9007, 1079-7114.
- [25] T. Ishikawa, K. Kato, M. Nomura, N. Suzuki, H. Nagara, and K. Shimizu, *Physical Review B* **88**, 214110 (2013).
- [26] R. Ahuja, S. Rekh, and B. Johansson, *Physical Review B* **63**, 212101 (2001).
- [27] J. C. Boettger, *Physical Review B* **67**, 174107 (2003).
- [28] X.-L. Z. Zhong-Li Liu, Ya-Ping Tao and L.-C. Cai, *Computational Materials Science* **114**, 72 (2016).
- [29] N. A. Smirnov, *J. Phys.: Condens. Matter* **29** (2017).
- [30] C. E. Rasmussen, *ArXiv* (2006), URL <https://arxiv.org/html/2102.05497>.
- [31] P. Vinet, J. Ferrante, J. H. Rose, and J. R. Smith, *Journal of Geophysical Research: Solid Earth* **92**, 9319 (1987), <https://agupubs.onlinelibrary.wiley.com/doi/pdf/10.1029/JB092iB09p09319>, URL

<https://agupubs.onlinelibrary.wiley.com/doi/abs/10.1029/JB092iB09p09319>.

- [32] S. Zhang, M. C. Marshall, L. H. Yang, P. A. Sterne, B. Militzer, M. Däne, J. A. Gaffney, A. Shamp, T. Ogitsu, K. Caspersen, et al., *Phys. Rev. E* **102**, 053203 (2020), URL <https://link.aps.org/doi/10.1103/PhysRevE.102.053203>.
- [33] B. Militzer, F. González-Cataldo, S. Zhang, K. P. Driver, and F. S. Soubiran, *Phys. Rev. E* **103**, 013203 (2021), URL <https://link.aps.org/doi/10.1103/PhysRevE.103.013203>.
- [34] L. H. Yang, R. Q. Hood, J. E. Pask, and J. E. Klepeis, *Journal of Computer-Aided Materials Design* **14**, 337 (2007), ISSN 1573-4900, URL <https://doi.org/10.1007/s10820-007-9053-1>.
- [35] P. Giannozzi, S. Baroni, N. Bonini, M. Calandra, R. Car, C. Cavazzoni, D. Ceresoli, G. L. Chiarotti, M. Cococcioni, I. Dabo, et al., *Journal of Physics: Condensed Matter* **21**, 395502 (2009), URL <https://dx.doi.org/10.1088/0953-8984/21/39/395502>.
- [36] J. Perdew and A. Zunger, *Physical Review B* **23**, 5048 (1981), ISSN 0163-1829.
- [37] J. P. Perdew, K. Burke, and M. Ernzerhof, *Phys. Rev. Lett.* **77**, 3865 (1996), URL <https://link.aps.org/doi/10.1103/PhysRevLett.77.3865>.
- [38] J. P. Perdew, K. Burke, and M. Ernzerhof, *Physical Review Letters* **78**, 1396 (1997).
- [39] A. V. Terentjev, L. A. Constantin, and J. M. Pitarke, *Phys. Rev. B* **98**, 214108 (2018), URL <https://link.aps.org/doi/10.1103/PhysRevB.98.214108>.
- [40] A. Dal Corso, *Physical Review B* **82**, 075116 (2010).
- [41] A. Dal Corso, *Physical Review B* **86**, 085135 (2012).
- [42] T. Tadano and S. Tsuneyuki, *Phys. Rev. B* **92**, 054301 (2015), URL <https://link.aps.org/doi/10.1103/PhysRevB.92.054301>.
- [43] D. R. Hamann, *Phys. Rev. B* **88**, 085117 (2013), URL <https://link.aps.org/doi/10.1103/PhysRevB.88.085117>.
- [44] J. Pask, private communication (2023).
- [45] J. R. Neighbours and G. A. Alers, *Phys. Rev.* **111**, 707 (1958), URL <https://link.aps.org/doi/10.1103/PhysRev.111.707>.
- [46] L. H. Yang, P. Söderlind, D. C. Swift, and J. A. Gaffney, unpublished (2024).
- [47] F. Zhou, W. Nielson, Y. Xia, and V. Ozoliņš, *Phys. Rev. B* **100**, 184308 (2019), URL <https://link.aps.org/doi/10.1103/PhysRevB.100.184308>.
- [48] K. Kusaba and T. Kikegawa, *Solid State Communications* **149**, 371 (2009), ISSN 0038-1098, URL <https://www.sciencedirect.com/science/article/pii/S0038109808007187>.
- [49] R. Nagai, R. Akashi, and O. Sugino, *npj Computational Materials* **6**, 43 (2020), ISSN 2057-3960, URL <https://doi.org/10.1038/s41524-020-0310-0>.
- [50] R. Christensen, T. Bligaard, and K. W. Jacobsen, in *Uncertainty Quantification in Multiscale Materials Modeling*, edited by Y. Wang and D. L. McDowell (Woodhead Publishing, 2020), Elsevier Series in Mechanics of Advanced Materials, pp. 77-91, ISBN 978-0-08-102941-1, URL <https://www.sciencedirect.com/science/article/pii/B9780081029411000031>.

- [51] K. Lejaeghere, in *Uncertainty Quantification in Multiscale Materials Modeling*, edited by Y. Wang and D. L. McDowell (Woodhead Publishing, 2020), Elsevier Series in Mechanics of Advanced Materials, pp. 41–76, ISBN 978-0-08-102941-1, URL <https://www.sciencedirect.com/science/article/pii/B978008102941100002X>.
- [52] F. Gygi, *Journal of Chemical Theory and Computation* **19**, 1300 (2023), ISSN 1549-9618, doi: 10.1021/acs.jctc.2c01191, URL <https://doi.org/10.1021/acs.jctc.2c01191>.
- [53] P. Söderlind, private communication (2023).

IX. APPENDIX: HANDLING INPUT AND OUTPUT NOISE WITH SQUARED EXPONENTIAL KERNELS

At their core, GPs define a prior over functions and, given data, infer a posterior function space that captures the underlying data-generating process [6, 30]. The kernel or covariance function characterizes the smoothness and variation of these functions, embodying the GP’s assumption about the data correlation. EIV-GPs [9–12] address this by modeling the noise directly in the observations that a local linear Taylor expansion about each input point is used. This approach allows the input noise to be reformulated as output noise proportional to the squared gradient of the GP posterior mean. The EIV-GP approach is described as follows:

Given a pair of measurements \mathbf{X} and \mathbf{y} , where \mathbf{X} is a D -dimensional input and \mathbf{y} is the corresponding scalar output, we have:

$$\mathbf{y} = \tilde{\mathbf{y}} + \epsilon_y$$

$$\mathbf{X} = \tilde{\mathbf{X}} + \epsilon_x$$

with $\epsilon_y \sim \mathcal{N}(0, \sigma_y^2)$ and $\epsilon_x \sim \mathcal{N}(0, \Sigma_x)$, where Σ_x is diagonal since each input dimension is assumed to be independently corrupted by noise.

Under the GP model, the output as a function of the input is given by:

$$\mathbf{y} = f(\tilde{\mathbf{X}} + \epsilon_x) + \epsilon_y$$

However, due to the noise in the inputs, we consider a Taylor expansion around the latent state $\tilde{\mathbf{X}}$, which leads to:

$$f(\tilde{\mathbf{X}} + \epsilon_x) \approx f(\tilde{x}) + \epsilon_x^T \nabla_{\tilde{\mathbf{X}}} f(\tilde{\mathbf{X}})$$

The derivative of a GP is another GP thus we can express the probability of an observation y given the function f

as:

$$P(y|f) = \mathcal{N}(f, \sigma_y^2 + \nabla f^T \Sigma_x \nabla f)$$

, where $\nabla f \equiv \nabla_{\tilde{\mathbf{X}}} f(\tilde{\mathbf{X}})$ is the gradient of the GP function value for the D -dimensional input. The predictive posterior mean and variance for a new input x^* are then given by:

$$\begin{aligned} \mathbb{E}[f^*|\mathbf{X}, y, x^*] &= k(x^*, \mathbf{X})[K(\mathbf{X}, \mathbf{X}) + \sigma_y^2 I + \\ &\quad \text{diag}(\nabla f \Sigma_x \nabla f^T)]^{-1} y \end{aligned}$$

$$\begin{aligned} \text{Var}[f^*|\mathbf{X}, y, x^*] &= k(x^*, x^*) - k(x^*, \mathbf{X})[K(\mathbf{X}, \mathbf{X}) + \\ &\quad \sigma_y^2 I + \text{diag}(\nabla f \Sigma_x \nabla f^T)]^{-1} k(\mathbf{X}, x^*), \end{aligned}$$

where k denotes the covariance function, K is the covariance matrix based on the training inputs \mathbf{X} , and σ_y^2 is the noise variance in the outputs. The notation diag results in a diagonal matrix whose elements come from its matrix argument.

Training involves an iterative scheme that alternates between optimizing the hyperparameters via the maximization of the marginal likelihood and calculating the posterior gradient.

$$\begin{aligned} \log P(\mathbf{y}|\mathbf{X}, \theta) &= -\frac{1}{2} \mathbf{y}^\top (K + \sigma_y^2 I)^{-1} \mathbf{y} \\ &\quad - \frac{1}{2} \log |K + \sigma_y^2 I| - \frac{n}{2} \log(2\pi) \end{aligned}$$

, where \mathbf{X} denotes the matrix of inputs, \mathbf{y} the vector of outputs, K the covariance matrix, and θ the hyperparameters. This procedure accounts for both input and output noise in the GP, leading to a robust model capable of making predictions at noisy input locations with a reasonable computational load.

The formulation of the derivative of a GP with input and output noise is central to the EOS thermodynamic properties, such as thermal pressure and specific heat, where the derivatives of free energies are subject to uncertainty. Here, we will provide the formulation of the exact mean and covariance of the predictive distribution of the latent function f and its gradient ∇f at an uncertain input \mathbf{X} .

The squared exponential (SE) covariance function is defined as:

$$K_{\sigma_f, \Lambda}(\mathbf{X}, \mathbf{X}') = \sigma_f^2 \exp\left(-\frac{1}{2}(\mathbf{X} - \mathbf{X}')^T \Lambda^{-1}(\mathbf{X} - \mathbf{X}')\right)$$

, where Λ is typically a diagonal matrix of the length scales, λ_i , and σ_f^2 is the signal variance. Both Λ and σ_f^2 are optimized hyperparameters θ via the maximization of the marginal likelihood.

The derivatives of this kernel with respect to the inputs are given by:

$$K_{(10)}(\mathbf{X}, \mathbf{X}') = \nabla_{\mathbf{X}} K(\mathbf{X}, \mathbf{X}') = -\Lambda^{-1}(\mathbf{X} - \mathbf{X}')K(\mathbf{X}, \mathbf{X}')$$

$$K_{(01)}(\mathbf{X}, \mathbf{X}') = \nabla_{\mathbf{X}'} K(\mathbf{X}, \mathbf{X}') = (\mathbf{X} - \mathbf{X}')^T \Lambda^{-1} K(\mathbf{X}, \mathbf{X}')$$

$$K_{(11)}(\mathbf{X}, \mathbf{X}') = \nabla_{\mathbf{X}} (\nabla_{\mathbf{X}'} K(\mathbf{X}, \mathbf{X}'))$$

0 and 1 denote the zeroth- and first-order derivatives, respectively. When dealing with the mean and covariance of the latent function and its derivatives, the mean of the derivative, ∇f , at the uncertain input, is obtained by the rule of iterated expectations:

$$\mathbb{E}[\nabla f] = -\Lambda^{-1} \sum_{i=1}^N \alpha_i (\mathbb{E}[x_i^* K(\mathbf{X}, x_i^*)] - x_i^* \mathbb{E}[K(\mathbf{X}, x_i^*)])$$

Here, α is the vector of optimized weights from the GP posterior, and x_i^* denotes the i -th input to calculate the predictive mean $\frac{\partial f}{\partial x_i^*}$.

For the variance of the derivative, the total variance rule is applied:

$$\text{Var}[\nabla f] = \mathbb{E}_x[\text{Var}_f[\nabla f]] + \text{Var}_x[\mathbb{E}_f[\nabla f]]$$

The covariance between the latent function f and its derivative ∇f is given by:

$$\text{Cov}(f, \nabla f) = \Lambda^{-1} \sum_{i=1}^N \sum_{j=1}^N \alpha_i \alpha_j (\text{Cov}[K(X, x_i^*), K(X, x_j^*)])$$